ceramics

Article

Energy Storage Performance of $Na_{0.5}Bi_{0.5}TiO_3$–$CaHfO_3$ Lead-Free Ceramics Regulated by Defect Engineering

Zhuo Li *, Jing Zhang, Zixuan Wang, Xiaotian Wei, Dingjie Long, Xin Zhao and Yanhui Niu *

School of Materials Science and Engineering, Chang'an University, Xi'an 710061, China
* Correspondence: lizhuo@chd.edu.cn (Z.L.); niuyh@chd.edu.cn (Y.N.)

Abstract: Over the past decades, $Na_{0.5}Bi_{0.5}TiO_3$ (NBT)-based ceramics have received increasing attention in energy storage applications due to their high power density and relatively large maximum polarization. However, their high remnant polarization (P_r) and low breakdown field strength are detrimental for their practical applications. In this paper, a new solid solution $(1-x)Na_{0.5}Bi_{0.5}TiO_3$–$xCaHfO_3$ (x = 0.04, 0.08, 0.12, 0.16) was constructed by introducing $CaHfO_3$ into NBT, and thus was prepared using a conventional solid-state reaction. With the addition of $CaHfO_3$, the disorder of the structure increased, A-site vacancies formed, and thus oxygen vacancies were suppressed due to the replacement of the Na^+ by Ca^{2+}, resulting in the enhanced relaxation behavior and the reduced P_r, the refined grain, and improved breakdown strength. Furthermore, an optimal recoverable energy storage density (W_{rec}) of 1.2 J/cm^3 was achieved in $0.92Na_{0.5}Bi_{0.5}TiO_3$–$0.08CaHfO_3$ ceramics under the breakdown strength of 140 kV/cm, which is mainly attributed to the resultant defect of Na^+ vacancy.

Keywords: NBT; lead-free ceramics; defect engineering; energy storage density

Citation: Li, Z.; Zhang, J.; Wang, Z.; Wei, X.; Long, D.; Zhao, X.; Niu, Y. Energy Storage Performance of $Na_{0.5}Bi_{0.5}TiO_3$–$CaHfO_3$ Lead-Free Ceramics Regulated by Defect Engineering. *Ceramics* **2024**, *7*, 1002–1013. https://doi.org/10.3390/ceramics7030065

Academic Editor: Fanglin Chen

Received: 18 June 2024
Revised: 18 July 2024
Accepted: 24 July 2024
Published: 28 July 2024

Copyright: © 2024 by the authors. Licensee MDPI, Basel, Switzerland. This article is an open access article distributed under the terms and conditions of the Creative Commons Attribution (CC BY) license (https://creativecommons.org/licenses/by/4.0/).

1. Introduction

Due to their high power density and quick charge/discharge rate, dielectric capacitors have drawn more attention in recent decades in the field of energy and electricity, and electronic circuit systems [1,2]. Among them, ceramic-based dielectric materials have high breakdown field strength (E_b), low dielectric loss ($\tan(\delta)$), excellent fatigue resistance, and superior thermal stability, making them suitable in a variety of industries, including in oil exploration, aerospace, and military applications [3–5]. Usually, dielectric ceramic materials with large maximum polarization (P_{max}), small remnant polarization (P_r) and high E_b are perfect for creating energy storage capacitors, and energy storage performance can be evacuated by using the polarization-electric field (P-E) loop according to the subsequent Equations (1)–(3).

$$W_{tot} = \int_0^{P_{max}} EdP \tag{1}$$

$$W_{rec} = \int_{P_r}^{P_{max}} EdP \tag{2}$$

$$\eta = \frac{W_{rec}}{W_{tot}} \times 100\% = \frac{W_{rec}}{W_{rec} + W_{loss}} \times 100\% \tag{3}$$

where E, W_{tot}, W_{rec}, W_{loss}, and η denote the applied electric field, total energy storage density, recoverable energy storage density, energy loss density, and energy storage efficiency, respectively.

Although Pb-based ceramics exhibit excellent energy storage performance due to their larger P_{max} and higher E_b, the resultant heavy metal Pb due to the volatilization during high-temperature preparation process and the subsequent scrap of products all pose risks to the ecological environment and people's health [6,7]. Therefore, designing and researching lead-free materials are considered a feasible solution to solve this problem. In numerous lead-free dielectric ceramics, $Na_{0.5}Bi_{0.5}TiO_3$ (NBT) based ceramics have attracted much attention on account of high Curie temperature (T_c) (~320 °C) and large saturation polarization strength (P_s, 45 $\mu C/cm^2$) [8]. However, the energy storage properties of NBT ceramics were dissatisfied because of the high Pr (~38 $\mu C/cm^2$). In addition, the elements Bi and Na are easily volatile during the process of high-temperature sintering, which may lead to the generation of cationic vacancies and oxygen vacancies, and thus the E_b reduced [9,10]. As a consequence, many researchers have focused on the settlement of these issues [11–21]. Thereinto, Yan et al. [12] prepared $0.75Bi_{(0.5+x)}Na_{(0.5-x)}TiO_3$–$0.25SrTiO_3$ ceramics by defect engineering and suppressed the formation of oxygen vacancies by adjusting the non-stoichiometric ratio of the A-site, as well as refined the grains size to increase E_b significantly. Eventually, the outstanding W_{rec} (~5.63 J/cm^3) and the relatively high η (~94%) were achieved under 569 kV/cm as x = 0.08. The $0.9(Na_{0.4}Bi_{0.4}Ba_{0.06}Sr_{0.14}Ti_{(1-x)}Ta_xO_3)$–$0.1NaNbO_3$ ceramics designed and prepared by Jiang et al. [13] effectively suppressed oxygen vacancies and increased the E_b through defect engineering and finally realized a relative high W_{rec} (~3.12 J/cm^3) and excellent η (~87.68%). By replacing Bi^{3+} and Na^+ at A-site with La^{3+} to increase the concentration of cation vacancies and decrease oxygen vacancies, the 0.85NBT–$0.15CaTiO_3$–0.75La ceramics showed the improved energy storage performance with W_{rec} of ~2.15 J/cm^3 and η of ~81% [16]. Apparently, the defect engineering modulation is an effective way to improve the energy storage performance of NBT-based ceramics.

In this study, by incorporating $CaHfO_3$ into NBT ceramics from a defect engineering perspective, a binary solid solution $Na_{0.5}Bi_{0.5}TiO_3$–$CaHfO_3$ was designed. On the one hand, the introduction of Ca^{2+} at A-site may induce the cation vacancies and thus significantly suppress oxygen vacancies, along with Hf^{4+} replacing Ti^{4+} in the B-site with a relatively strong bond strength of Hf–O, ultimately all improving the E_b. On the other hand, due to the incorporation of non-equivalent cations as Na^+, Ca^{2+}, and Bi^{3+}, the creation of a local random field may break the long-range order ferroelectric domain and facilitate the formation of polar nanoregions (PNRs), which contributed to the decrease of P_r [22–24]. On the basis of the above analysis, $(1-x)Na_{0.5}Bi_{0.5}TiO_3$–$xCaHfO_3$ (NBT–$xCaHfO_3$, x = 0.04, 0.08, 0.12, 0.16) solid solution was prepared using the conventional solid state method, and the phase structure, microstructure, dielectric properties and energy storage characteristics were investigated in detail. The ceramics designed and fabricated using this strategy are expected to be used in the field of pulsed power capacitors.

2. Experimental Procedures

$(1-x)Na_{0.5}Bi_{0.5}TiO_3$–$xCaHfO_3$ (NBT−$xCaHfO_3$, x = 0.04, 0.08, 0.12, 0.16) ceramics were prepared using a conventional solid phase method [25,26]. The starting materials including Na_2CO_3 (analytical reagent (AR), ≥ 99.8%), Bi_2O_3 (AR, ≥ 99.9%), TiO_2 (chemically pure, ≥ 98.0%), $CaCO_3$ (AR, ≥ 99.0%), and HfO_2 (AR, ≥ 98.0%), which were all from Sinopharm Chemical Reagent Co., Ltd., Shanghai, China, were weighed according to the stoichiometric ratio of their components. The weighed powders were ball milled for 8 h by using the alcohol as medium. After that, the mixture was dried in an oven before calcination in a muffle furnace at 850 °C for 2 h. Following that, the powder was ball milled for another 6 h, and then was dried and sieved. The sieved powder was granulated with 6% polyvinyl alcohol (PVA) and then pressed into disks with a diameter of 13 mm under a pressure of 300 MPa. Finally, the disks were heated to 550 °C at the speed of 3 °C/min for 3 h to remove the PVA, and then sintered at 1100–1140 °C for 2 h at the rate of 5 °C/min to obtain the final ceramic samples.

X-ray diffraction (XRD, D8 Advanced, Bruker AXS Ltd., Karlsruhe, Germany) was used to analyze the crystal structure of the ceramic samples with diffraction angle 2θ in the range of 20–80°, and the accurate crystal structure of the ceramic materials were obtained using Rietveld full diffraction patterns fitting. The microstructures of the ceramic samples were observed using field emission scanning electron microscopy (SEM, S-4800, Hitachi, Japan). As for electrical testing, the ceramic samples were polished into a thickness of

~1 mm, covered with silver paste on the top and bottom surfaces, and then were fired at 850 °C for 10 min to form the electrodes. The LCR impedance meter (E4294A, Agilent, Santa Clara, USA) was used to measure the dielectric properties in the temperature range of 25–400 °C with a frequency in the range of 1 kHz to 1 MHz. In addition, the P-E curves of ceramic samples under different electric field strength were tested using a ferroelectric analyzer (TF2000, AixACCT, Aachen, Germany).

3. Results and Discussions

The XRD patterns of the NBT–x$CaHfO_3$ (x = 0.04, 0.08, 0.12, 0.16) ceramics sintered at the optimum temperature are shown in Figure 1a. As can be seen from this Figure, the X-ray diffraction patterns of all ceramic component exhibited a single perovskite structure, and no second phases were detected, which indicated that $CaHfO_3$ was completely diffused into the NBT lattice and formed a perfect solid solution. Figure 1b,c present the magnified plots of the diffraction peaks near 40.2° and 46.8° to further investigate the structural evolution of the ceramics. It can be seen that a significant splitting presented in both peaks near 40.2° and 46.8°, confirming that all ceramics were in the coexistence of the rhombohedral phase (R3c) and the tetragonal phase (P4bm) at room temperature [27]. The two split diffraction peaks weakened and merged gradually when $CaHfO_3$ content increased, which demonstrated that the coexistence of R3c and P4bm phases had evolved into a pseudo-cubic phase [28,29]. In addition, as $CaHfO_3$ doping content increased, the diffraction peaks were first shifted to higher angles (in particular, x = 0.12 is the most prominent), confirming the decreased cell volumes owing to the smaller radius Ca^{2+} (1.34 Å) replacing the larger radius Na^{+} (1.39 Å). However, due to the limited solid solubility of the A-site, when $CaHfO_3$ doping content exceeds the threshold, the Ti^{4+} (0.605 Å) with a smaller radius at the B-site could be replaced by Ca^{2+} (1.34 Å) [30], and at the same time, more Hf^{4+} (0.71 Å) with a larger radius enters the B-site to replace Ti^{4+}, resulting in lattice volume expansion and diffraction peaks shifting towards small angles. In addition, the bulk density of NBT–x$CaHfO_3$ (x = 0.04, 0.08, 0.12, 0.16) ceramics sintered at different temperatures was plotted in Figure 1d. The bulk density of NBT–x$CaHfO_3$ increased initially with increasing sintering temperatures and then decreased after reaching the maximum value. It should be noted that the sintering temperature of the maximum bulk density was 1120 °C for all the different compositions.

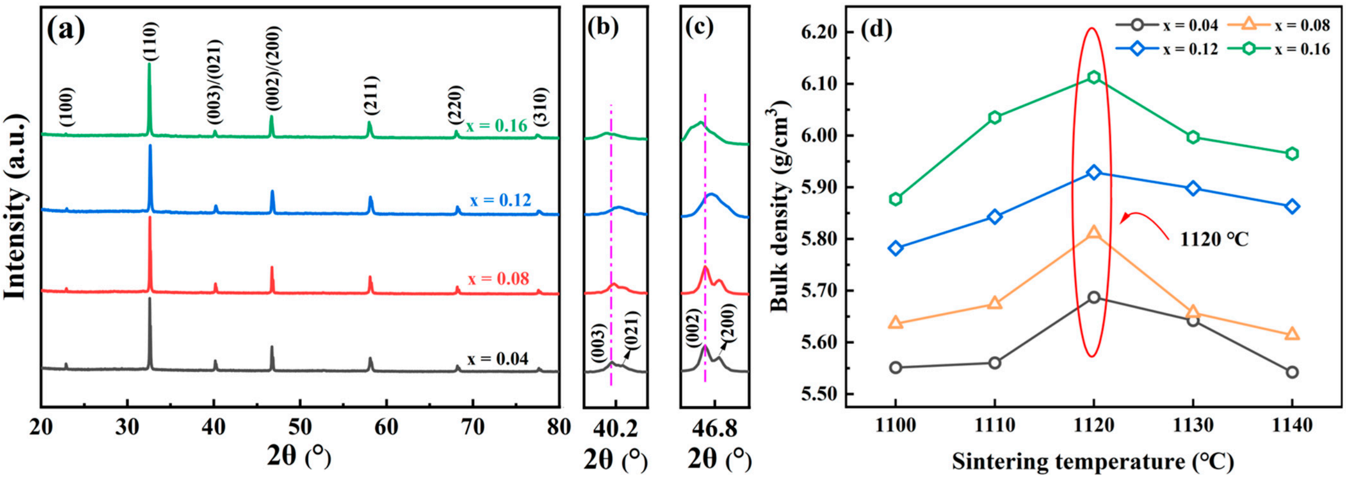

Figure 1. (**a**) XRD pattern of NBT–x$CaHfO_3$ (x = 0.04, 0.08, 0.12, 0.16) ceramics. The magnified view at 2θ (**b**) near 40.2° and (**c**) near 46.8°. (**d**) The bulk density of NBT–x$CaHfO_3$ ceramics sintered at different temperatures.

In order to further analyze the effect of $CaHfO_3$ doping on the phase structure and lattice parameters of the NBT–x$CaHfO_3$ ceramics, Figure 2 presents the Rietveld refinement of the full-scan XRD diffraction patterns based on the R3c and P4bm phase, and the corresponding phase proportion, lattice parameters, and reliability factors are shown in

Table 1. The reliability factors of weighted patterns (R_{wp}) and the goodness-of-fit indicator (χ^2) of all component ceramics are within the confidence interval, confirming that the results of XRD refinement are relatively reliable. Clearly, the fraction of the P4bm phase first increased and then decreased with the increase in $CaHfO_3$ content, as x = 0.08 reached the maximum. Usually, P4bm as the weakly polar phase could be converted into a polar ferroelectric state under an electric field and return to the original weakly polar state when the electric field was removed, hence the enhancement proportion of the P4bm phase could contribute to the reduction in P_r and thus promote the energy storage properties [31,32]. It can be assumed that the NBT–0.08$CaHfO_3$ ceramics may have optimal energy storage performance accompanied with relatively low P_r.

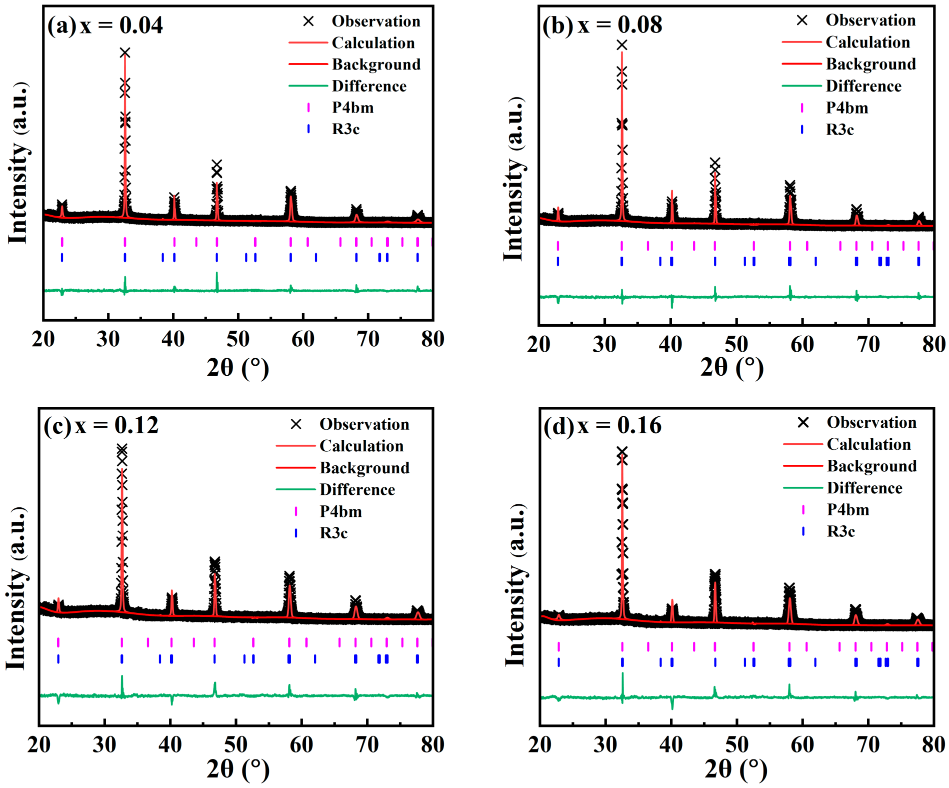

Figure 2. Rietveld Refined XRD Patterns of NBT–x$CaHfO_3$ ceramics: (**a**) x = 0.4, (**b**) x = 0.08, (**c**) x = 0.12, and (**d**) x = 0.16.

Table 1. The refinement results from full-diffraction pattern fitting of NBT–x$CaHfO_3$ ceramics.

x	Phase Structure	Relative Content (%)	Lattice Parameters			Reliability Factor	
			a(Å)	b(Å)	c(Å)	Rwp (%)	χ2
0.04	R3c P4bm	37.30% 62.70%	5.497 5.500	5.497 5.500	13.478 3.887	8.4%	1.76
0.08	R3c P4bm	7.47% 92.53%	5.497 5.503	5.497 5.503	13.494 3.889	8.7%	1.83
0.12	R3c P4bm	28.26% 71.74%	5.495 5.500	5.495 5.500	13.502 3.892	8.8%	2.26
0.16	R3c P4bm	22.85% 77.15%	5.494 5.507	5.494 5.507	13.520 3.895	9.4%	2.28

Figure 3 shows the natural surface micrographs of NBT–x$CaHfO_3$ ceramics. All samples present clear grain morphology and a relatively dense microstructure. In order to further investigate the effect of $CaHfO_3$ doping on the microscopic morphology of NBT ceramics, the average grain (AG) sizes of each component ceramics were analyzed, as shown in Figure 4. The average grain size of the ceramics decreased from 3.14 μm for x = 0.04 to 1.35 μm for x = 0.12, verifying that the addition of $CaHfO_3$ could refine grain size to a certain extent. Since Ca^{2+} tended to displace Na^+ at A-site due to the similar ionic radii ($R_{Ca}{}^{2+}$ = 1.34 Å, $R_{Na}{}^{+}$ = 1.39 Å), and thus produced cation defects with positive charges, denoted as $Ca_{Na}^{\bullet}$ [32,33], and Na^+ vacancies (expressed as V'_{Na}) for charge compensation and for maintaining electrical neutrality. Consequently, the oxygen vacancy ($V_O^{\bullet\bullet}$), created by loss of oxygen from the crystal lattice at low oxygen partial pressure during sintering at high temperatures had to be inhabited [13,34,35], which further suppressed the conductivity and refined the grain size as well as beneficial to the enhancement of the E_b [36,37]. Furthermore, with the $CaHfO_3$ increasing, more V'_{Na} favor the mass transfer in ceramics during sintering [13,38], and as a consequence, the grain size increased up to 1.40 μm when x = 0.16. The equation for the defect is as follows (Equations (4) and (5)), in which the Kröger–Vink notation was employed.

$$CaO \overset{Na_2O}{\rightarrow} Ca_{Na}^{\bullet} + V'_{Na} + O_O \quad (4)$$

$$O_O \rightarrow V_O^{\bullet\bullet} + e' \quad (5)$$

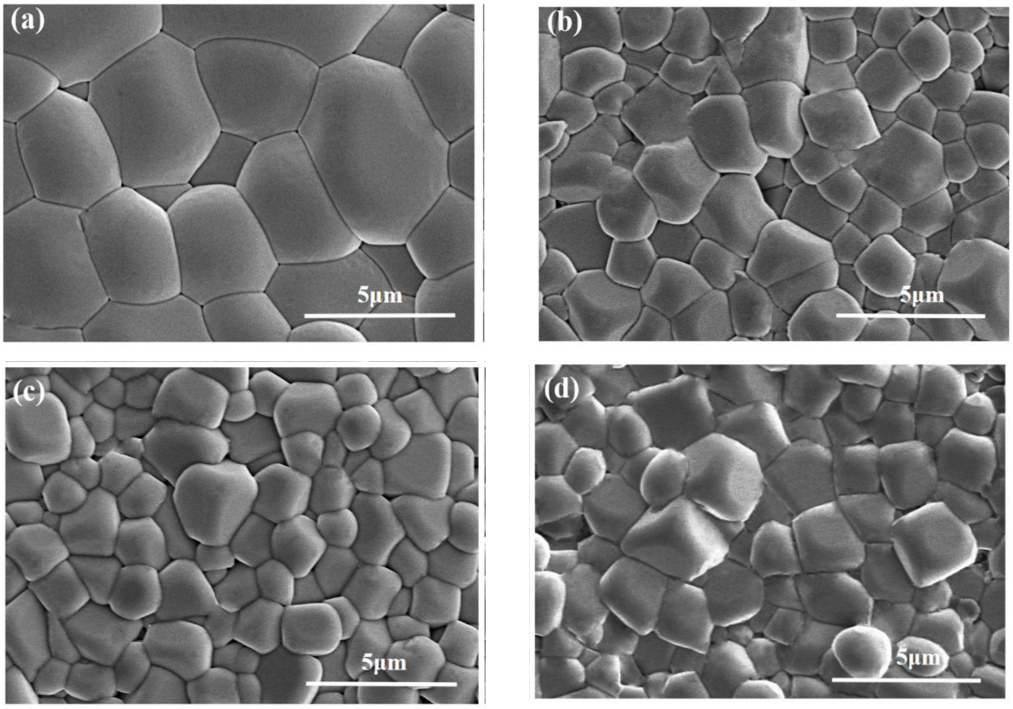

Figure 3. SEM images of NBT–x$CaHfO_3$ ceramics: (**a**) x = 0.4, (**b**) x = 0.08, (**c**) x = 0.12, and (**d**) x = 0.16.

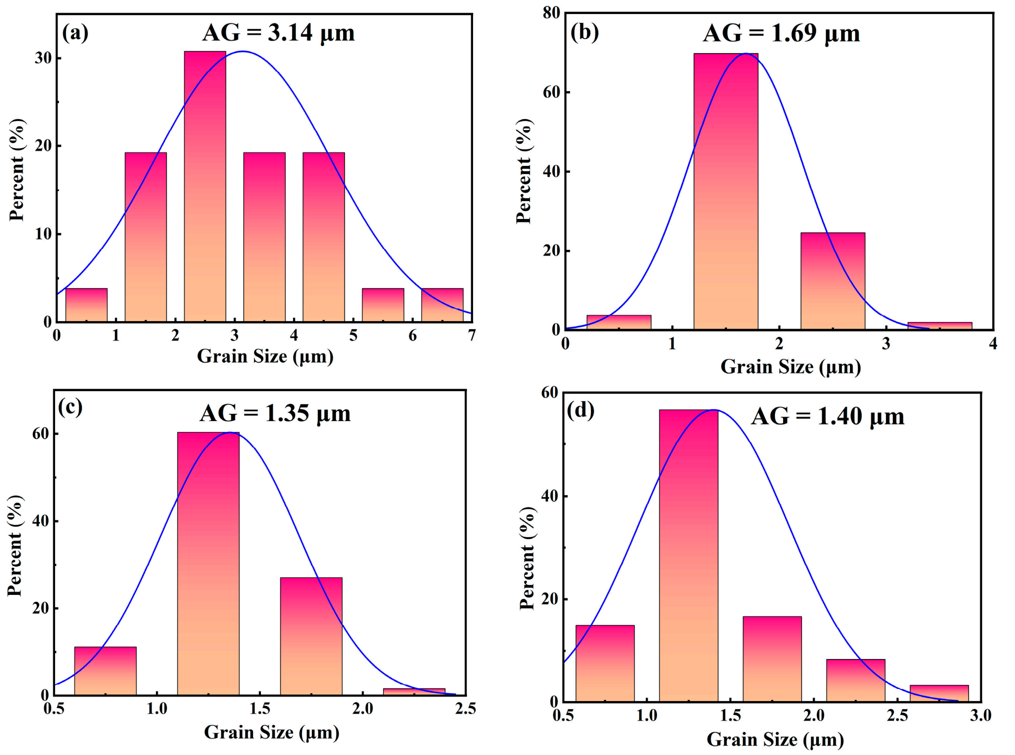

Figure 4. Grain size distribution diagram of NBT–xCaHfO$_3$ ceramics: (**a**) x = 0.4, (**b**) x = 0.08, (**c**) x = 0.12, (**d**) x = 0.16.

Figure 5 shows the variation curves of dielectric constant (ε_r) and dielectric loss (tan(δ)) under different frequency for NBT–xCaHfO$_3$ ceramics. The ε_r of all ceramics presents a decreasing trend to a different extent with the frequency increased, which may be due to the inability of defect dipoles to respond at high frequencies [39,40]. Besides that, when the CaHfO$_3$ content increased, ε_r at the frequency of 10 kHz decreased from 811 for the composition of x = 0.04 to 606 (x = 0.08) and then increased sharply to 1066 (x = 0.12), accomplished by the minimum dielectric loss (tan(δ) less than 0.022) emerging in the composition of x = 0.08 in a wide range of frequencies from 1k Hz to 1 MHz, implying that the appropriate amount of CaHfO$_3$ can reduce the concentration of oxygen vacancies and decrease the dielectric loss, which is conducive to the enhancement of the breakdown field strength. Figure 6 illustrates the temperature-dependent dielectric properties of NBT–xCaHfO$_3$ (x = 0.04, 0. 08, 0.12, and 0.16) ceramics at various frequencies. The dielectric anomaly peak (T_m) clearly observed refers to the ferro-paraelectric phase transition [41,42]. It is noteworthy that with the increase of CaHfO$_3$ content, the dielectric peak became flatter and broader, accompanied by the T_m shifting to the lower temperature, which may be caused by the diminished coupling effect of [TiO$_6$] octahedron and weakened structure stability, since A-site vacancies (V'_{Na}) formed as excessively Ca^{2+} doped [43,44]. In the meantime, as the frequency increased from 1 kHz to 1 MHz, ε_r decreased steadily and T_m shifted to the higher temperature, manifesting a relaxed behavior to a certain extent [45]. To further analyze the effect of CaHfO$_3$ content on the degree of relaxation, the diffuseness parameter γ between 1 (normal ferroelectric) and 2 (ideal relaxer) was calculated using the modified Curie–Weiss equation (Equation (6)) [46–48]:

$$\frac{1}{\varepsilon_r}-\frac{1}{\varepsilon_m}=\frac{(T-T_m)^{\gamma}}{C} \tag{6}$$

where *C* represents the Curie–Weiss constant and ε_m is the dielectric constant corresponding to T_m. The γ obtained by fitting the curves between ln(T$-$T$_m$) and ln((1/ε_r)$-$(1/ε_m)) at 1 kHz, as shown in Figure 7, increased from 1.44 (x = 0.04) to 1.63 (x = 0.08) and then decreased to 1.57 (x = 0.12) and 1.54 (x = 0.16), hinting that the optimal relaxation characteristics can be obtained in the composition of x = 0.08. The optimizing relaxation performance may be related to the increased ionic disorder in the microstructure, where the non-equivalent substitution of Ca^{2+} for Na^+ and Bi^{3+} broke the long-range ferroelectric domains and facilitated the formation of polar nanoregions [49–51].

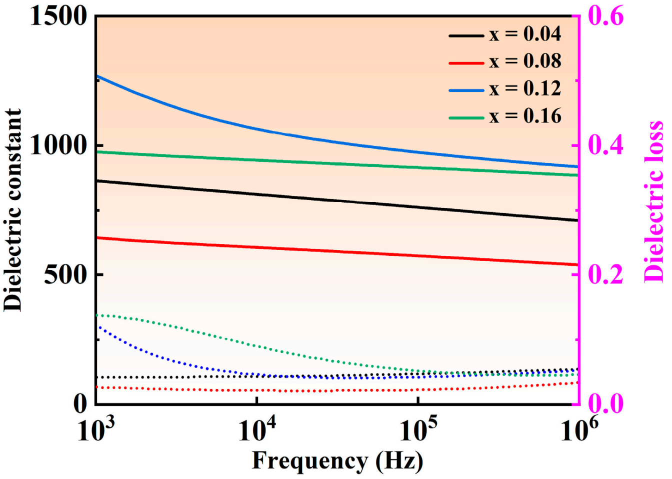

Figure 5. Frequency-dependent dielectric properties of NBT–x$CaHfO_3$ (x = 0.04, 0.08, 0.12, 0.16) ceramics at room temperature. Solid lines signify dielectric constant and dashed lines denote dielectric loss.

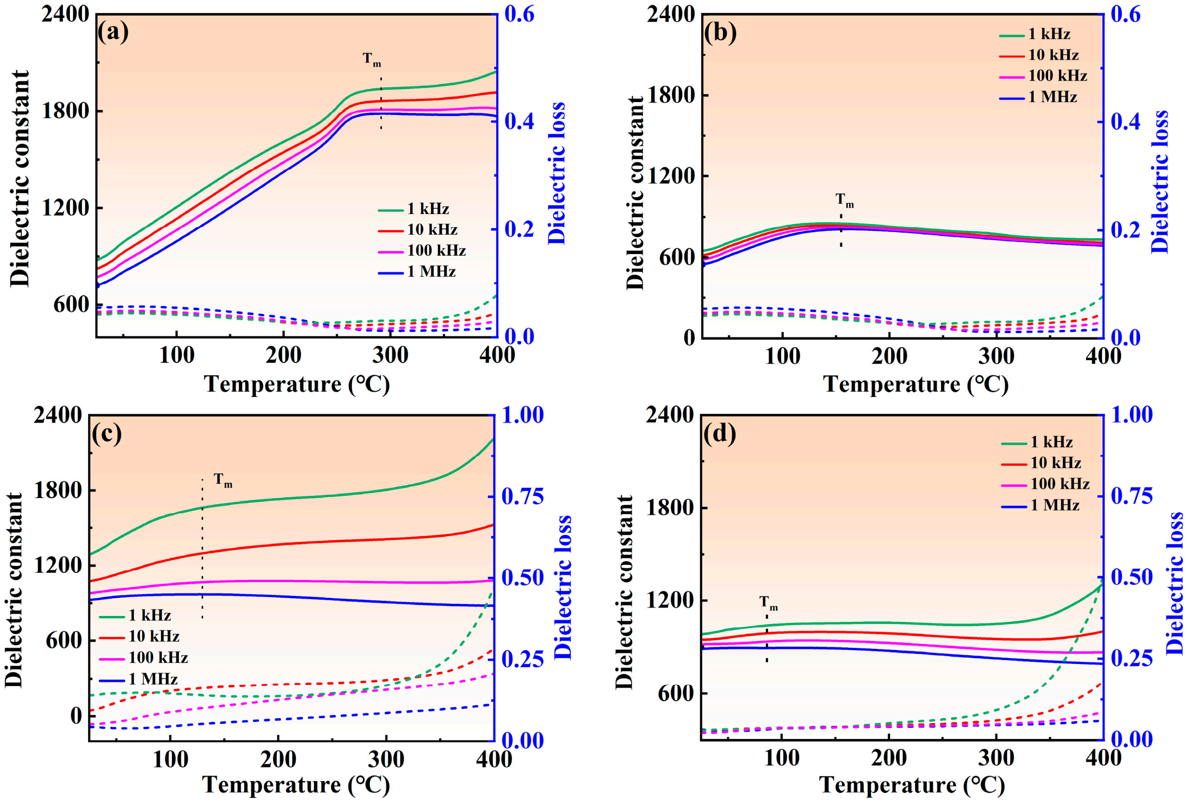

Figure 6. Temperature-dependent dielectric properties of NBT–x$CaHfO_3$ ceramics under various frequencies: (**a**) x = 0.04, (**b**) x = 0.08, (**c**) x = 0.12, and (**d**) x = 0.16. Solid lines signify dielectric constant and dashed lines denote dielectric loss.

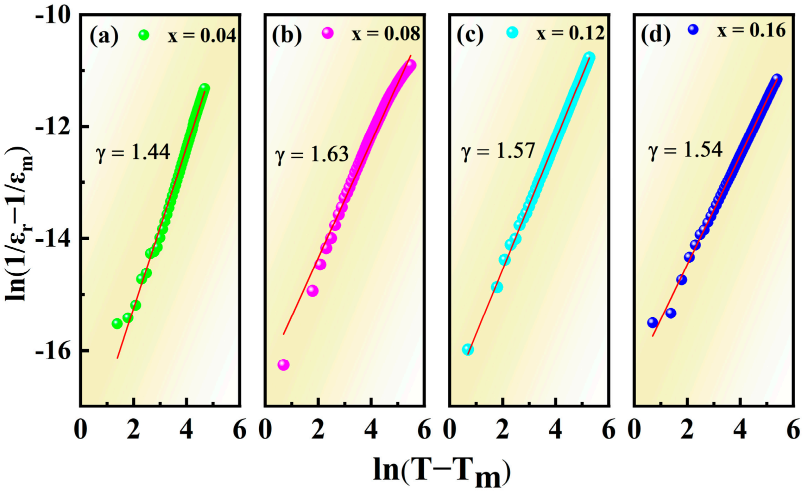

Figure 7. $\ln((1/\varepsilon_r)-(1/\varepsilon_m))$ as a function of $\ln(T-T_m)$ for NBT–xCaHfO$_3$ ceramics: (**a**) x = 0.04, (**b**) x = 0.08, (**c**) x = 0.12, and (**d**) x = 0.16. (solid lines—fitting to Equation (6)).

Figure 8 displays the P-E hysteresis loops of NBT–xCaHfO$_3$ ceramics under the electric fields of 120 kV/cm. Evidently, as CaHfO$_3$ content increases, the P-E loops become slimmer, especially for the NBT–0.08CaHfO$_3$ ceramics, which is in agreement with the result of diffuseness parameter γ. The slender P-E loops can be mainly ascribed to the broken long-range ferroelectric domain as the non-equivalent substitution of Na$^+$ and Bi^{3+} by Ca^{2+}. Thus, the formed polar microregions suppressed the early polarization saturation of the ceramics and reduced the P_r, which facilitated the achievement of excellent energy storage performance [24,52]. In addition, Figure 9 displays the P-E hysteresis loops of NBT–xCaHfO$_3$ ceramics under various electric fields. Apparently, P-E loops of all composition turn more slender with increasing applied electric filed, among which P_{max} and ΔP ($\Delta P = P_{max}-P_r$) of the composition with x = 0.08 increases significantly, while P_r increases slightly. Ultimately, under an electric fields of 140 kV/cm, P_{max} and ΔP reach their maximums, as displayed in the inset of Figure 9b.

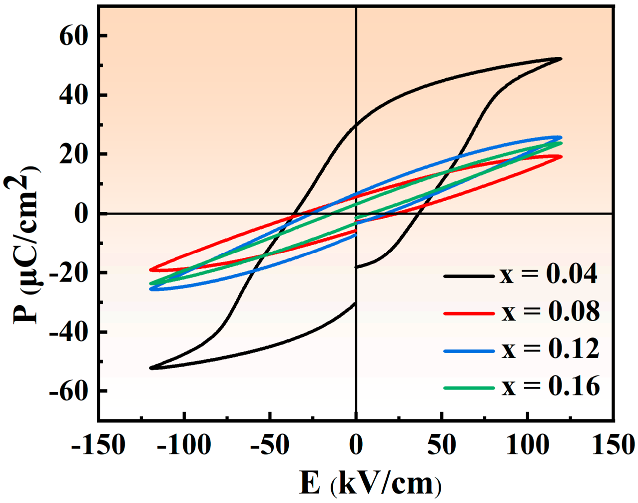

Figure 8. P-E curves of NBT–xCaHfO$_3$ ceramic samples under the electric field of 120 kV/cm.

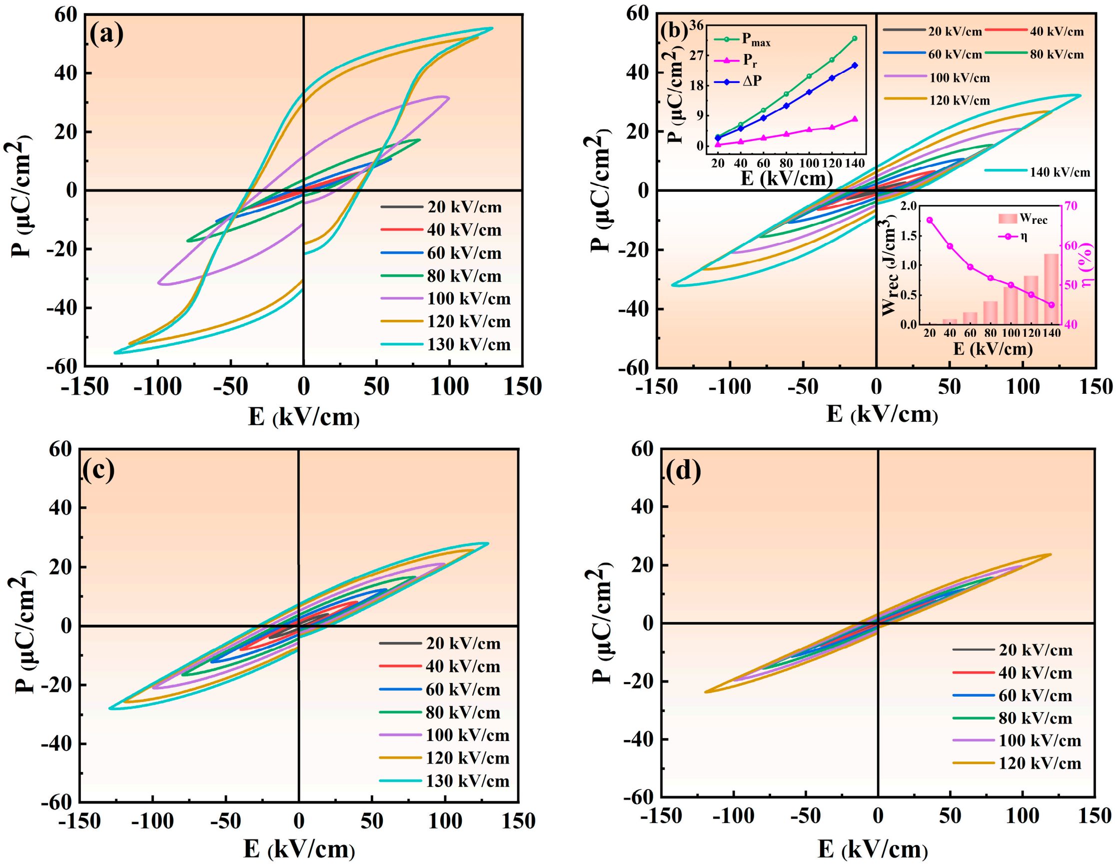

Figure 9. P-E curves of NBT–x$CaHfO_3$ ceramic samples under different electric field: (**a**) x = 0.04, (**b**) x = 0.08, (**c**) x = 0.12, and (**d**) x = 0.16.

The improvement of W_{rec} requires not only high P_{max} and low P_r, but also high applied field and, subsequently, the P-E hysteresis loops of NBT–x$CaHfO_3$ ceramics at 20 Hz under critical electric fields are displayed in Figure 10a. Compared to NBT–x$CaHfO_3$ ceramics with x = 0.04, 0.12, and 0.16, the NBT–0.08$CaHfO_3$ ceramics demonstrated the maximum E_b value of 140 kV/cm because of the dense microstructure and relatively small grain size (in Figure 3). The variation of W_{rec}, η and P_{max}, P_r, and ΔP for each ceramic under a critical electric field are shown in Figure 10b,c, and the relevant parameters are listed in Table 2. Overall, with the increase in the $CaHfO_3$ content, the P_{max} decreased from 55.39 μC/cm^2 (x = 0.04) to 23.66 μC/cm^2 (x = 0.16) together with P_r maintaining in a relatively low value. Finally, the ΔP attained its maximum for NBT–0.08$CaHfO_3$ ceramics, achieving the optimizing energy storage performance with W_{rec} of 1.2 J/cm^3 and η of 45%. Also, the energy storage performance and polarization properties of NBT–0.08$CaHfO_3$ ceramics under various electric fields from 20 kV/cm to 140 kV/cm are demonstrated in the inset of Figure 9b. Apparently, ΔP enhanced approximately linearly from 2.33 μC/cm^2 to 24.12 μC/cm^2, with the increase in applied electric field as a result of the significant increase of P_{max} along with a slight increase of P_r. The comparatively large ΔP and E_b facilitated excellent energy storage properties. Hence, the W_{rec} of 1.20 J/cm^3 was highlighted in 0.92NBT–0.08$CaHfO_3$ ceramics under the maximum electric field of 140 kV/cm, indicating certain potential in energy storage application.

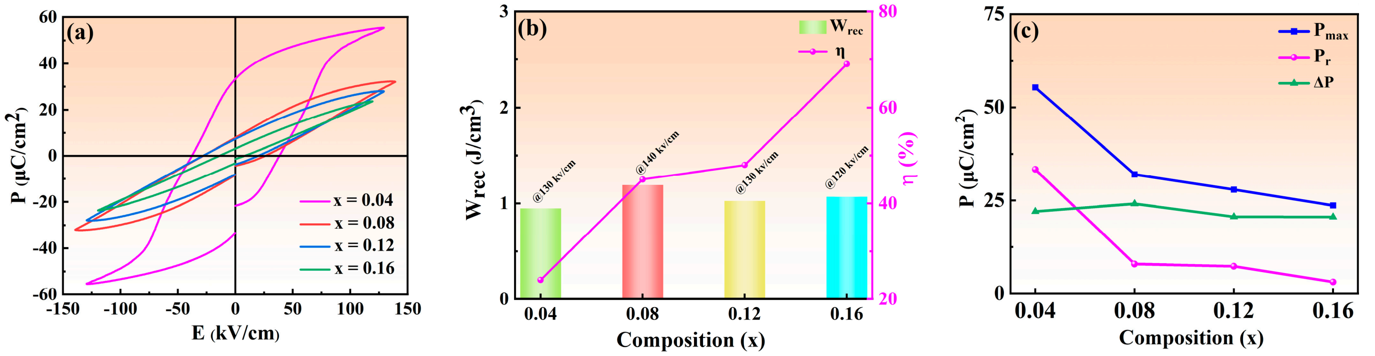

Figure 10. (**a**) P-E curves, (**b**) W_{rec} and η, (**c**) P_{max}, P_r, and ΔP of NBT–$xCaHfO_3$ ceramic samples under critical electric field.

Table 2. P_{max}, P_r, W_{rec}, and η of NBT–$xCaHfO_3$ ceramics under the critical electric field.

x	E_b (kV/cm)	P_{max} (μC/cm^2)	P_r (μC/cm^2)	W_{rec} (J/cm^3)	η (%)
0.04	130	55.39	33.30	0.95	24%
0.08	140	32.10	7.88	1.20	45%
0.12	130	27.93	7.31	1.03	48%
0.16	120	23.66	3.09	1.07	69%

4. Conclusions

NBT–$xCaHfO_3$ (x = 0.04, 0.08, 0.12, 0.16) ceramics were prepared using a conventional solid phase method. The introduction of Ca^{2+} substituting for Na^+ and Bi^{3+} at the A-site induced the cation vacancies and then suppressed the concentration of oxygen vacancies as well as refined the grain size, associated with Hf $^{4+}$ replacing Ti^{4+} in the B-site with a relatively strong bond strength of Hf–O, eventually fulfilling the improvement of the E_b. Besides that, a local random field created by the incorporation of non-equivalent cations as Na^+, Ca^{2+}, Bi^{3+}, and cation vacancies, as well as bond strength of Hf–O, broke the long-range order ferroelectric domain and facilitated the formation of PNRs, resulting in an enhancement of relaxation properties and a decrease in P_r. Combined with enhanced relaxation behavior and increased E_b, an optimizing W_{rec} of 1.2 J/cm^3 was achieved in NBT–$0.08CaHfO_3$ ceramics under the E_b of 140 kV/cm. All of these demonstrated that the NBT–$0.08CaHfO_3$ ceramics have an attractive potential in the field of energy storage ceramics.

Author Contributions: Conceptualization, Z.L.; methodology, J.Z.; formal analysis, Z.L. and D.L.; investigation, X.W., D.L. and X.Z.; resources, Y.N.; data curation, X.Z. and Y.N.; writing—original draft, J.Z.; writing—review and editing, Z.L. and Z.W. All authors have read and agreed to the published version of the manuscript.

Funding: This research was funded by the Fundamental Research Funds for the Central Universities, CHD (No. 300102314904), the Natural Science Foundation of Shaanxi province, China (No. 2021JM-172) and the National Natural Science Foundations of China (Grant No. 52278427).

Data Availability Statement: The original contributions presented in the study are included in the article, further inquiries can be directed to the corresponding author.

Conflicts of Interest: The authors declare no conflicts of interest.

References

1. Yang, Z.; Du, H.; Jin, L.; Poelman, D. High-Performance Lead-Free Bulk Ceramics for Electrical Energy Storage Applications: Design Strategies and Challenges. *J. Mater. Chem. A* **2021**, *9*, 18026–18085. [CrossRef]
2. Palneedi, H.; Peddigari, M.; Hwang, G.; Jeong, D.; Ryu, J. High-Performance Dielectric Ceramic Films for Energy Storage Capacitors: Progress and Outlook. *Adv. Funct. Mater.* **2018**, *28*, 1803665. [CrossRef]
3. Yuan, Q.; Chen, M.; Zhan, S.; Li, Y.; Lin, Y.; Yang, H. Ceramic-Based Dielectrics for Electrostatic Energy Storage Applications: Fundamental Aspects, Recent Progress, and Remaining Challenges. *Chem. Eng. J.* **2022**, *446*, 136315.

4. Hu, Q.; Tian, Y.; Zhu, Q.; Bian, J.; Jin, L.; Du, H.; Alikin, D.O.; Shur, V.Y.; Feng, Y.; Xu, Z.; et al. Achieve Ultrahigh Energy Storage Performance in $BaTiO_3$–$Bi(Mg_{1/2}Ti_{1/2})O_3$ Relaxor Ferroelectric Ceramics via Nano-Scale Polarization Mismatch and Reconstruction. *Nano Energy* **2020**, *67*, 104264.
5. Muhammad, R.; Iqbal, Y.; Reaney, I.M. $BaTiO_3$–$Bi(Mg_{2/3}Nb_{1/3})O_3$ Ceramics for High-Temperature Capacitor Applications. *J. Am. Ceram. Soc.* **2016**, *99*, 2089–2095. [CrossRef]
6. Wang, H.; Liu, Y.; Yang, T.; Zhang, S. Ultrahigh Energy-Storage Density in Antiferroelectric Ceramics with Field-Induced Multiphase Transitions. *Adv. Funct. Mater.* **2019**, *29*, 1807321. [CrossRef]
7. Wang, H.; Hu, Q.; Liu, X.; Zheng, Q.; Jiang, N.; Yang, Y.; Kwok, K.W.; Xu, C.; Lin, D. A High-Tolerance BNT-Based Ceramic with Excellent Energy Storage Properties and Fatigue/Frequency/Thermal Stability. *Ceram. Int.* **2019**, *45*, 23233–23240.
8. Wang, G.; Lu, Z.; Li, Y.; Li, L.; Ji, H.; Feteira, A.; Zhou, D.; Wang, D.; Zhang, S.; Reaney, I.M. Electroceramics for High-Energy Density Capacitors: Current Status and Future Perspectives. *Chem. Rev.* **2021**, *121*, 6124–6172. [CrossRef] [PubMed]
9. Höfling, M.; Steiner, S.; Hoang, A.-P.; Seo, I.-T.; Frömling, T. Optimizing the Defect Chemistry of $Na_{1/2}Bi_{1/2}TiO_3$ -Based Materials: Paving the Way for Excellent High Temperature Capacitors. *J. Mater. Chem. C* **2018**, *6*, 4769–4776. [CrossRef]
10. Carter, J.; Aksel, E.; Iamsasri, T.; Forrester, J.S.; Chen, J.; Jones, J.L. Structure and Ferroelectricity of Nonstoichiometric $(Na_{0.5}Bi_{0.5})TiO_3$. *Appl. Phys. Lett.* **2014**, *104*, 112904. [CrossRef]
11. Yang, H.; Cai, Z.; Zhu, C.; Feng, P.; Wang, X. Ultra-High Energy Storage Performance in BNT-Based Ferroelectric Ceramics with Simultaneously Enhanced Polarization and Breakdown Strength. *ACS Sustain. Chem. Eng.* **2022**, *10*, 9176–9183. [CrossRef]
12. Yan, F.; Huang, K.; Jiang, T.; Zhou, X.; Shi, Y.; Ge, G.; Shen, B.; Zhai, J. Significantly Enhanced Energy Storage Density and Efficiency of BNT-Based Perovskite Ceramics via A-Site Defect Engineering. *Energy Storage Mat.* **2020**, *30*, 392–400. [CrossRef]
13. Jiang, Z.; Yang, H.; Cao, L.; Yang, Z.; Yuan, Y.; Li, E. Enhanced Breakdown Strength and Energy Storage Density of Lead-Free $Bi_{0.5}Na_{0.5}TiO_3$-Based Ceramic by Reducing the Oxygen Vacancy Concentration. *Chem. Eng. J.* **2021**, *414*, 128921. [CrossRef]
14. Zhang, L.; Jing, R.; Huang, Y.; Hu, Q.; Alikin, D.O.; Shur, V.Y.; Gao, J.; Wei, X.; Zhang, L.; Liu, G.; et al. Enhanced Antiferroelectric-like Relaxor Ferroelectric Characteristic Boosting Energy Storage Performance of $(Bi_{0.5}Na_{0.5})TiO_3$-Based Ceramics via Defect Engineering. *J. Mat.* **2022**, *8*, 527–536. [CrossRef]
15. Liu, G.; Dong, J.; Zhang, L.; Yu, L.; Wei, F.; Li, Y.; Gao, J.; Hu, J.; Yan, Y.; Li, Q.; et al. $Na_{0.25}Sr_{0.5}Bi_{0.25}TiO_3$ Relaxor Ferroelectric Ceramic with Greatly Enhanced Electric Storage Property by a B-Site Ion Doping. *Ceram. Int.* **2020**, *46*, 11680–11688. [CrossRef]
16. Yu, L.; Dong, J.; Tang, M.; Liu, Y.; Wu, F.; Yan, Y.; Liu, G.; Song, C. Enhanced Electrical Energy Storage Performance of Pb-Free A-Site La^{3+}-Doped $0.85Na_{0.5}Bi_{0.5}TiO_3$-$0.15CaTiO_3$ Ceramics. *Ceram. Int.* **2020**, *46*, 28173–28182. [CrossRef]
17. Li, T.; Chen, P.; Si, R.; Li, F.; Guo, Y.; Wang, C. High Energy Storage Density and Efficiency with Excellent Temperature and Frequency Stabilities under Low Operating Field Achieved in $Ag_{0.91}Sm_{0.03}NbO_3$-Modified $Na_{0.5}Bi_{0.5}TiO_3$-$BaTiO_3$ Ceramics. *J. Mater. Sci. Mater. Electron.* **2020**, *31*, 16928–16937. [CrossRef]
18. Liu, X.; Rao, R.; Shi, J.; He, J.; Zhao, Y.; Liu, J.; Du, H. Effect of Oxygen Vacancy and A-Site-Deficiency on the Dielectric Performance of BNT-BT-BST Relaxors. *J. Alloys Compd.* **2021**, *875*, 159999. [CrossRef]
19. Chen, Z.; Pu, Y.; Ning, Y.; Hui, Y.; Wu, C.; Zhang, L.; Zhang, X.; Wang, B. Prominent Energy Storage Density and Efficiency of $Na_{0.5}Bi_{0.5}TiO_3$ -based Ceramics via Multiscale Amelioration Strategy. *J. Am. Ceram. Soc.* **2024**, *107*, 2360–2370. [CrossRef]
20. Zhao, H.; Cao, W.; Liang, C.; Wang, C.; Wang, C. High Energy-Storage Performance in X9R-Type $Na_{0.5}Bi_{0.5}TiO_3$-Based Lead-Free Ceramics. *Ceram. Int.* **2023**, *49*, 15939–15946. [CrossRef]
21. Li, T.; Jiang, X.; Li, J.; Xie, A.; Fu, J.; Zuo, R. Ultrahigh Energy-Storage Performances in Lead-Free $Na_{0.5}Bi_{0.5}TiO_3$ -Based Relaxor Antiferroelectric Ceramics through a Synergistic Design Strategy. *ACS Appl. Mater. Interfaces* **2022**, *14*, 22263–22269. [CrossRef] [PubMed]
22. Roukos, R.; Zaiter, N.; Chaumont, D. Relaxor Behaviour and Phase Transition of Perovskite Ferroelectrics-Type Complex Oxides $(1–x)Na_{0.5}Bi_{0.5}TiO_3$–$xCaTiO_3$ System. *J. Adv. Ceram.* **2018**, *7*, 124–142. [CrossRef]
23. Luo, C.; Feng, Q.; Luo, N.; Yuan, C.; Zhou, C.; Wei, Y.; Fujita, T.; Xu, J.; Chen, G. Effect of Ca^{2+}/Hf^{4+} Modification at A/B Sites on Energy-Storage Density of $Bi_{0.47}Na_{0.47}Ba_{0.06}TiO_3$ Ceramics. *Chem. Eng. J.* **2021**, *420*, 129861. [CrossRef]
24. Wang, K.; Li, W.; Zhao, R.; Tang, X.; Zhang, S.; Zhang, Y.; Hu, J.; Shen, Z.; Jiang, Y.; Guo, X. High Energy Storage Density Obtained by $Bi(Ni_{0.5}Hf_{0.5})O_3$-Modified NBT-Based Ceramic at a Low Electric Field. *Ceram. Int.* **2024**, *50*, 5276–5284. [CrossRef]
25. Li, Z.; Zhang, J.; Wang, C.; Wang, Z.; Lei, N.; Zheng, L.; Long, D.; Wei, X.; Zhang, J.; Wang, Z.; et al. Phase Structure, Dielectric and Energy Storage Properties of $Na_{0.5}Bi_{0.5}TiO_3$-$BaTiO_3$ Ceramics with $Bi(Mg_{2/3}Nb_{1/3})O_3$ Modification. *Ceram. Int.* **2023**, *49*, 38735–38742. [CrossRef]
26. Zhang, L.; Pu, Y.; Chen, M.; Wei, T.; Keipper, W.; Shi, R.; Guo, X.; Li, R.; Peng, X. High Energy-Storage Density under Low Electric Fields and Improved Optical Transparency in Novel Sodium Bismuth Titanate-Based Lead-Free Ceramics. *J. Eur. Ceram. Soc.* **2020**, *40*, 71–77. [CrossRef]
27. Yang, F.; Bao, S.; Zhai, Y.; Zhang, Y.; Su, Z.; Liu, J.; Zhai, J.; Pan, Z. Enhanced Energy-Storage Performance and Thermal Stability in $Bi_{0.5}Na_{0.5}TiO_3$-Based Ceramics through Defect Engineering and Composition Design. *Mater. Today Chem.* **2021**, *22*, 100583. [CrossRef]
28. Qiao, X.; Wu, D.; Zhang, F.; Niu, M.; Chen, B.; Zhao, X.; Liang, P.; Wei, L.; Chao, X.; Yang, Z. Enhanced Energy Density and Thermal Stability in Relaxor Ferroelectric $Bi_{0.5}Na_{0.5}TiO_3$-$Sr_{0.7}Bi_{0.2}TiO_3$ Ceramics. *J. Eur. Ceram. Soc.* **2019**, *39*, 4778–4784. [CrossRef]

29. Yang, L.; Kong, X.; Cheng, Z.; Zhang, S. Ultra-High Energy Storage Performance with Mitigated Polarization Saturation in Lead-Free Relaxors. *J. Mater. Chem. A* **2019**, *7*, 8573–8580. [CrossRef]
30. Zhao, P.; Tang, B.; Si, F.; Yang, C.; Li, H.; Zhang, S. Novel Ca Doped $Sr_{0.7}Bi_{0.2}TiO_3$ Lead-Free Relaxor Ferroelectrics with High Energy Density and Efficiency. *J. Eur. Ceram. Soc.* **2020**, *40*, 1938–1946. [CrossRef]
31. Han, J.; Yin, J.; Wu, J. BNT-based Ferroelectric Ceramics: Electrical Properties Modification by Ta_2O_5 Oxide Addition. *J. Am. Ceram. Soc.* **2019**, *103*, 412–422. [CrossRef]
32. Fan, J.; He, G.; Cao, Z.; Cao, Y.; Long, Z.; Hu, Z. Ultrahigh Energy-Storage Density of a Lead-Free $0.85Bi_{0.5}Na_{0.5}TiO_3 - 0.15Ca(Nb_{0.5}Al_{0.5})O_3$ Ceramic under Low Electric Fields. *Inorg. Chem. Front.* **2023**, *10*, 1561–1573. [CrossRef]
33. Xie, A.; Fu, J.; Zuo, R.; Zhou, C.; Qiao, Z.; Li, T.; Zhang, S. $NaNbO_3$-$CaTiO_3$ Lead-Free Relaxor Antiferroelectric Ceramics Featuring Giant Energy Density, High Energy Efficiency and Power Density. *Chem. Eng. J.* **2022**, *429*, 132534. [CrossRef]
34. Prasertpalichat, S.; Cann, D.P. Hardening in Non-Stoichiometric $(1-x)Bi_{0.5}Na_{0.5}TiO_3$–$xBaTiO_3$ Lead-Free Piezoelectric Ceramics. *J. Mater. Sci.* **2016**, *51*, 476–486. [CrossRef]
35. Kumar, N.; Ansell, T.Y.; Cann, D.P. Role of Point Defects in Bipolar Fatigue Behavior of $Bi(Mg_{1/2}Ti_{1/2})O_3$ Modified $(Bi_{1/2}K_{1/2})TiO_3$-$(Bi_{1/2}Na_{1/2})TiO_3$ Relaxor Ceramics. *J. Appl. Phys.* **2014**, *115*, 154104. [CrossRef]
36. Li, M.; Pietrowski, M.J.; De Souza, R.A.; Zhang, H.; Reaney, I.M.; Cook, S.N.; Kilner, J.A.; Sinclair, D.C. A Family of Oxide Ion Conductors Based on the Ferroelectric Perovskite $Na_{0.5}Bi_{0.5}TiO_3$. *Nat. Mater.* **2014**, *13*, 31–35. [CrossRef]
37. Malik, R.A.; Hussain, A.; Maqbool, A.; Zaman, A.; Song, T.K.; Kim, W.-J.; Kim, M.-H. Giant Strain, Thermally-Stable High Energy Storage Properties and Structural Evolution of Bi-Based Lead-Free Piezoceramics. *J. Alloys Compd.* **2016**, *682*, 302–310. [CrossRef]
38. Zhu, X.; Gao, Y.; Shi, P.; Kang, R.; Kang, F.; Qiao, W.; Zhao, J.; Wang, Z.; Yuan, Y.; Lou, X. Ultrahigh Energy Storage Density in $(Bi_{0.5}Na_{0.5})_{0.65}Sr_{0.35}TiO_3$-Based Lead-Free Relaxor Ceramics with Excellent Temperature Stability. *Nano Energy* **2022**, *98*, 107276. [CrossRef]
39. Ding, J.; Pan, Z.; Chen, P.; Hu, D.; Yang, F.; Li, P.; Liu, J.; Zhai, J. Enhanced Energy Storage Capability of $(1-x)Na_{0.5}Bi_{0.5}TiO_3$-$xSr_{0.7}Bi_{0.2}TiO_3$ Free-Lead Relaxor Ferroelectric Thin Films. *Ceram. Int.* **2020**, *46*, 14816–14821. [CrossRef]
40. Zhang, L.; Hao, X.; Zhang, L. Enhanced Energy-Storage Performances of Bi_2O_3–Li_2O Added $(1-x)(Na_{0.5}Bi_{0.5})TiO_3$–$xBaTiO_3$ Thick Films. *Ceram. Int.* **2014**, *40*, 8847–8851. [CrossRef]
41. Wang, H.; Yuan, H.; Li, X.; Zeng, F.; Wu, K.; Zheng, Q.; Fan, G.; Lin, D. Enhanced Energy Density and Discharged Efficiency of Lead-Free Relaxor $(1-x)[(Bi_{0.5}Na_{0.5})_{0.94}Ba_{0.06}]_{0.98}La_{0.02}TiO_3$-$xKNb_{0.6}Ta_{0.4}O_3$ Ceramic Capacitors. *Chem. Eng. J.* **2020**, *394*, 124879. [CrossRef]
42. Huang, J.; Qi, H.; Gao, Y.; Xie, A.; Zhang, Y.; Li, Y.; Wang, S.; Zuo, R. Expanded Linear Polarization Response and Excellent Energy-Storage Properties in $(Bi_{0.5}Na_{0.5})TiO_3$-$KNbO_3$ Relaxor Antiferroelectrics with Medium Permittivity. *Chem. Eng. J.* **2020**, *398*, 125639. [CrossRef]
43. Li, D.; Lin, Y.; Zhang, M.; Yang, H. Achieved Ultrahigh Energy Storage Properties and Outstanding Charge–Discharge Performances in $(Na_{0.5}Bi_{0.5})_{0.7}Sr_{0.3}TiO_3$-Based Ceramics by Introducing a Linear Additive. *Chem. Eng. J.* **2020**, *392*, 123729. [CrossRef]
44. Li, X.; Cheng, Y.; Wang, F.; Xu, Q.; Chen, Y.; Xie, L.; Tan, Z.; Xing, J.; Zhu, J. Enhancement of Energy Storage and Hardness of $(Na_{0.5}Bi_{0.5})_{0.7}Sr_{0.3}TiO_3$-Based Relaxor Ferroelectrics via Introducing $Ba(Mg_{1/3}Nb_{2/3})O_3$. *Chem. Eng. J.* **2022**, *431*, 133441. [CrossRef]
45. Luo, C.; Wei, Y.; Feng, Q.; Wang, M.; Luo, N.; Yuan, C.; Zhou, C.; Fujita, T.; Xu, J. Significantly Enhanced Energy-Storage Properties of $Bi_{0.47}Na_{0.47}Ba_{0.06}TiO_3$-$CaHfO_3$ Ceramics by Introducing $Sr_{0.7}Bi_{0.2}TiO_3$ for Pulse Capacitor Application. *Chem. Eng. J.* **2022**, *429*, 132165. [CrossRef]
46. Yan, F.; Zhou, X.; He, X.; Bai, H.; Wu, S.; Shen, B.; Zhai, J. Superior Energy Storage Properties and Excellent Stability Achieved in Environment-Friendly Ferroelectrics via Composition Design Strategy. *Nano Energy* **2020**, *75*, 105012. [CrossRef]
47. Jiang, Z.; Yuan, Y.; Yang, H.; Li, E.; Zhang, S. Relaxor Regulation and Improvement of Breakdown Strength for $Bi_{0.5}Na_{0.5}TiO_3$-Based Ceramics by Co-Doping with Ca and Nb. *Ceram. Int.* **2022**, *48*, 9702–9709. [CrossRef]
48. Meng, K.; Li, W.; Tang, X.; Liu, Q.; Jiang, Y. The Defect Related Energy-Storage Properties of A-Site off-Stoichiometry Ferroelectric Ceramic. *Appl. Phys. A* **2021**, *127*, 337. [CrossRef]
49. Huang, Y.; Zhang, L.; Jing, R.; Hu, Q.; Alikin, D.O.; Shur, V.Y.; Islam, S.S.; Du, H.; Wei, X.; Feng, G.; et al. Thermal Stability of Dielectric and Energy Storage Performances of Ca-Substituted BNTZ Ferroelectric Ceramics. *Ceram. Int.* **2021**, *47*, 6298–6309. [CrossRef]
50. Krogstad, M.J.; Gehring, P.M.; Rosenkranz, S.; Osborn, R.; Ye, F.; Liu, Y.; Ruff, J.P.C.; Chen, W.; Wozniak, J.M.; Luo, H.; et al. The Relation of Local Order to Material Properties in Relaxor Ferroelectrics. *Nat. Mat.* **2018**, *17*, 718–724. [CrossRef]
51. Wang, Z.; Kang, R.; Zhang, L.; Mao, P.; Sun, Q.; Kang, F.; Wang, J. Remarkably Enhanced Energy-Storage Density and Excellent Thermal Stability under Low Electric Fields of $(Na_{0.5}Bi_{0.5})TiO_3$-Based Ceramics via Composition Optimization Strategy. *J. Eur. Ceram. Soc.* **2021**, *41*, 1917–1924. [CrossRef]
52. Li, X.; Dong, X.; Wang, F.; Tan, Z.; Zhang, Q.; Chen, H.; Xi, J.; Xing, J.; Zhou, H.; Zhu, J. Realizing Excellent Energy Storage Properties in $Na_{0.5}Bi_{0.5}TiO_3$-Based Lead-Free Relaxor Ferroelectrics. *J. Eur. Ceram. Soc.* **2022**, *42*, 2221–2229. [CrossRef]

Disclaimer/Publisher's Note: The statements, opinions and data contained in all publications are solely those of the individual author(s) and contributor(s) and not of MDPI and/or the editor(s). MDPI and/or the editor(s) disclaim responsibility for any injury to people or property resulting from any ideas, methods, instructions or products referred to in the content.